



A new visible band index (vNDVI) for estimating NDVI values on RGB images utilizing genetic algorithms

Lucas Costa, Leon Nunes, Yiannis Ampatzidis*

Agricultural and Biological Engineering Department, Southwest Florida Research and Education Center, University of Florida, IFAS, 2685 SR 29 North, Immokalee, FL 34142, USA



ARTICLE INFO

Keywords:

Genetic algorithm
Big data
NDVI
Vegetation index
RGB
Multispectral
Hyperspectral

ABSTRACT

Several vegetation indices have been developed, with the normalized difference vegetation index (NDVI) been the most studied and commonly used. To generate an NDVI map, a relatively high-cost multispectral sensor is required; but currently, most UAVs are equipped with low-cost RGB cameras. For that reason, other indices that utilize RGB data have been developed to generate maps similar to NDVI and minimize the data acquisition cost, such as the triangular greenness index (TGI) and the visible atmospheric resistant index (VARI). However, several studies found that these indices cannot be recommended as reliable general-purpose crop health indicators. This study utilizes a genetic algorithm to develop a new visible index (visible NDVI; vNDVI) that estimates NDVI values of vegetation from uncalibrated RGB cameras mounted on UAVs (or other remote sensing platforms). Three experiments were conducted to create and validate the proposed index. First, the NDVI values generated from a multispectral camera were compared with the NDVI values generated by a hyperspectral camera. In the second experiment, the vNDVI formula was created using a genetic algorithm. The third experiment validates the proposed vNDVI, generated from two uncalibrated RGB cameras, in three different crops (citrus, grapes, and sugarcane). The proposed vNDVI proved to be highly accurate on estimating NDVI values by just using RGB cameras, with an overall mean percentage error of 6.89% and a mean average error of 0.052 in all three crops, providing a low-cost alternative for remote sensing and plant phenotyping.

1. Introduction

Enormous efforts are being applied to analyze plant genetics and develop crop varieties with high yield, environmental stress tolerance, and disease resistance (Cuenca et al., 2013; Rambla et al., 2014). Breeding analysis requires many years to be implemented in order to develop, select, and release new crop varieties (Sahin-Çevik and Moore, 2012). A key point on new breeding programs is the creation of a huge amount of genetically diverse training population (Aleza et al., 2012). Traditional sensing methods for phenotypic analysis rely on manual sampling and are very labor-intensive and time consuming (Mahlein, 2016; Shakoor et al., 2017; Cruz et al., 2019). Furthermore, field surveys are important for plant inventory, plant health analysis, and pest and disease detection, which are also labor-intensive and time-consuming processes (Luvisi et al., 2016; Cruz et al., 2017; Partel et al., 2019a,b).

The use of remote sensing systems like satellite imagery, small airplanes, and unmanned aerial vehicles (UAVs) together with big data analytics and artificial intelligence (AI) provide new tools for plant

phenotyping (LeCun et al., 2015; Kussul et al., 2017). In agriculture, there has been a rising demand in remote sensing for its capabilities of collecting data in a shorter time with less manual labor and minor impact on the fields. For example, Wulder et al. (2004) proposed a method to compare the results of identification of individual trees on using the airborne Imaging Sensor II (MEIS II) and the IKONOS satellite. Santoro et al. (2013) proposed another procedure for individual fruit tree identification using GeoEye-1, utilizing a four-step algorithm that showed consistent results in fast capturing tree positions, but suffered when detecting trees of different varieties and ages, as well as in high-density tree spacing.

UAVs using a variety of different sensors are becoming a flexible and cost-effective solution for a rapid and accurate non-destructive crop analysis (Malek et al., 2014; Pajares, 2015; Singh et al., 2016). Crommelinck et al. (2017) showed that UAVs can cover areas at much lower heights generating high resolution images while keeping a low operation cost (Franzé et al., 2017). Ampatzidis et al. (2019) utilized UAVs and AI to evaluate citrus rootstock varieties, and Abdulridha et al. (2019a) and Harihara et al. (2019) developed UAV-based early disease

* Corresponding author.

E-mail address: i.ampatzidis@ufl.edu (Y. Ampatzidis).

detection systems for citrus and avocado utilizing hyperspectral imagery.

Several vegetation indices (VIs) have been developed, from UAV (or other remote sensing platforms) collected data, for plant phenotyping, including indices to assess plant health status, plant water status or water stress, and for disease detection (Ampatzidis et al., 2017; Abdulridha et al., 2019b,c). A vegetation index represents a combination or a filtering process of multiple spectral data sets to create a single value for each point in an image, generated usually by a mathematical model and used to develop a scale color map (McKinnon and Hoff, 2017). One of the most commonly used and studied vegetation index is the normalized difference vegetation index (NDVI) (Rouse et al., 1973). Initially, the NDVI was developed to generate a good correlation between NDVI values and grassland vegetation data (e.g., dry and green biomass) (Rouse et al., 1973).

Hunt et al. (2010) analyzed UAV multispectral imagery to monitor crops, and a good correlation between leaf area index and green NDVI (Gitelson and Merzlyak, 1996) was found. A vineyard vigor map was proposed by Matese et al. (2013) utilizing the NDVI, calculated with a high-resolution multispectral camera. Besides the healthy status index, the NDVI can provide, for each plant, specific features that can be used for plant detection, as proposed by Ampatzidis et al. (2019). NDVI has been used for many different purposes as spatial referencing, crop and climate monitoring, attribute mapping and in several decision support systems (Panda et al., 2010; Abdulridha et al., 2018).

To generate an NDVI map, a multispectral sensor operating in the near infrared (NIR) wavelength is required. However, multispectral cameras are usually more expensive than RGB cameras, and require time-consuming calibration procedures. Currently, conventional RGB cameras with high resolution are available from several manufacturers and the majority of UAVs are equipped with standard RGB cameras (Rabatel et al., 2011). Therefore, several plant indices were created using just conventional RGB channels to make the data collection more accessible.

Arai et al. (2016) proposed a method for NIR reflectance estimation utilizing visible cameras, achieving a high correlation between green reflectance and NIR reflectance. Using the concepts of ARVI (Kaufman and Tanre, 1992) to reduce atmospheric effects over the vegetation index computed using visible range of spectrum, Gitelson et al. (2002) proposed the visible atmospheric resistant index (VARI), which was to be used for estimating the fraction of vegetation in a scene with low sensitivity to atmospheric effects. However, as pointed in Gitelson et al. (2002), reflectance from green vegetated surfaces is not so high and the difference between the reflectivity levels of visible channels are not higher than between NIR and red, used to get the NDVI. The triangular greenness index (TGI), presented by Hunt et al. (2013), uses the area of a triangle in the spectral features of chlorophyll region and was developed to facilitate the imagery acquisition using just RGB channels instead of multispectral channels, to generate a chlorophyll content index. The results using these indices did not show any trend in data tested by McKinnon and Hoff (2017), and neither the TGI nor VARI can be recommended as a reliable general-purpose crop health indicator (McKinnon and Hoff, 2017). Zhang et al. (2016) created the synthetic NDVI time series, obtained by sensor fusion of high resolution RGB and low resolution NDVI satellite imagery, to access NDVI information with higher ground resolution for grassland biomass estimation. The study used a support vector machine to create the resulting biomass index, which got a good correlation to above ground biomass.

In this study, a new methodology was developed to calculate an estimation for the NDVI, based just on the three channels of RGB conventional cameras, using UAV imaging. The equation proposed (visual NDVI; vNDVI) was created on a genetic algorithm that uses the correlation between the RGB channels and the NDVI, calculated with multispectral data. This index can be generated with data collected by a low-cost and high spatial resolution RGB cameras, providing an easier and accessible tool for plant phenotyping. It can also be used in satellite

images that usually provide low spatial resolution multispectral data and high spatial and temporal resolution RGB data.

2. Materials and method

2.1. Vegetation Indices: NDVI and VARI

NDVI (generated by multispectral cameras) and VARI (generated by RGB cameras) are some of the most commonly used indices for vegetation assessment. Considering that plants have a higher reflectance in the near infrared (NIR) bands and low reflectance in the red bands, the NDVI formula evaluates this difference as it is presented in Eq. (1) (Rouse et al., 1973). Rouse et al. (1973) showed a good correlation between the NDVI and grassland vegetation data (dry biomass, green biomass, and percent green estimates).

$$NDVI = \frac{NIR - Red}{NIR + Red} \quad (1)$$

To monitor the vegetation fraction of wheat canopies, Gitelson et al. (2002) proposed a VI based on the red and green wavelengths, as shown by the Eq. (2):

$$VI_{green} = \frac{R_{green} - R_{red}}{R_{green} + R_{red}} \quad (2)$$

Then, using the concept of ARVI to reduce the atmospheric effects (Kaufman and Tanre, 1992), assuming that the effect in the blue wavelengths is two times bigger than in the green and red wavelengths, the visible atmospheric resistant index (VARI) was generated by the subtraction of the blue wavelength from the denominator of Eq. (2). The VARI, shown in Eq. (3), is used for estimating the vegetation fraction in a scene with low sensitivity to atmospheric effects.

$$VARI = \frac{R_{GREEN} - R_{RED}}{R_{GREEN} + R_{RED} - R_{BLUE}} \quad (3)$$

The VARI is one of the most commonly used indices for collecting data from vegetation by utilizing only RGB cameras. It was not developed to predict NDVI values, but as an RGB-based crop index.

2.2. Genetic algorithm

In order to develop an NDVI based on RGB, named herein as a visible NDVI (vNDVI), a function that depends on these values (red, green, and blue bands) is needed. The proposed topography for the function is shown in Eq. (4), where red, green and blue are the normalized values of each spectrum for the image pixel. The weights (w) and camera coefficient (C) are the set of constants to be found. This formula was selected from manual trials of different topography.

$$vNDVI = F(\text{camera}, \text{red}, \text{green}, \text{blue}) = C * (\text{red}^{w1} * \text{green}^{w2} * \text{blue}^{w3}) \quad (4)$$

To find the weights for the vNDVI, a genetic algorithm (GA) was developed to identify an optimal function that could relate the data gathered. A GA is based on evolution of individuals, where individuals carry genes that are unique and represent them; a set of individuals form a population. For every generation there is a population with different individuals. The individuals best set for their environment are more likely to become parents, and their child can carry their best genes. The GA developed in this study uses each weight (C , $w1$, $w2$, $w3$) in the formula (Eq. (4)) as a gene, and each set of weights composes an individual. A set of solutions (individuals) are ranked for every generation using a fitness function, which gives a score for each individual, to select which are the best individuals. Fig. 1 shows the definition of the population for this study.

A GA can be separated in three steps: Initialization, Selection and Genetic operators. At the Initialization step (Fig. 2), a population of possible solutions is generated through small variations (mutations) on

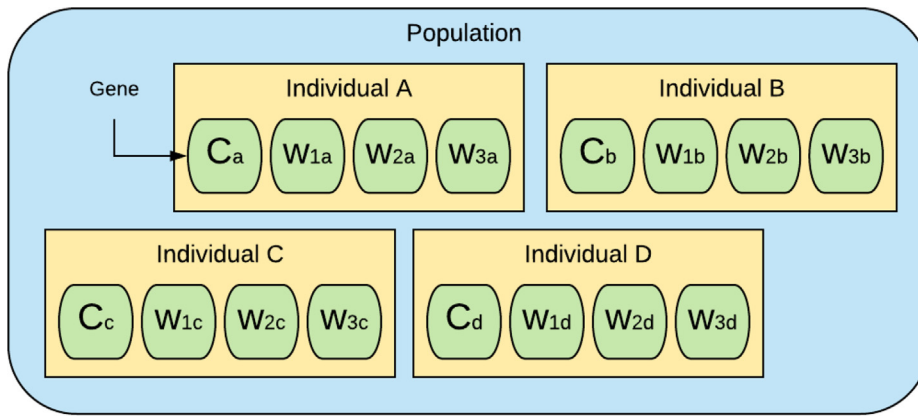


Fig. 1. An example of population for the GA developed, where each individual is a set of different genes.

a possible first individual, selected by the human operator. The mutation step is similar to the mutation process in the theory of evolution, where a new individual is created by small alterations of the genes of a parent individual. The algorithm that generates this mutation in the GA is exemplified on Eqs. (5) and (6), where individual A is the original solution, mutation is a set of random values ($\beta, \vartheta, \gamma, \chi$) to be randomly added to the original genes, and individual B is the generated solution from mutation.

$$\text{Individual } A = (CA, w1A, w2A, w3A); \text{ mutation} = (\beta, \vartheta, \gamma, \chi) \quad (5)$$

$$\begin{aligned} \text{Individual } B &= \text{Individual } A + \text{mutation } A \\ &= (CA + \beta, w1A + \vartheta, w2A + \gamma, w3A + \chi) \end{aligned} \quad (6)$$

Each successive population generated is selected through a fitness-based process, where a fitness function qualifies each single individual with a score. In this case, the fitness function is the mean error between the NDVI data and vNDVI data created by each individual (Eq. (7)). The

score (Eq. (8)) is calculated as the inverse of the fitness function, and is used to create a rank, and selects the best individuals of the population to continue to either advance to the next generation, create through genetic operation new individuals (as parents), or to be discarded. Fig. 3 shows the work flow for the selection step of the GA, where the population is organized by score to be used on the next step.

$$\text{Fitness function} = \text{Mean}(NDVI - vNDVI) \quad (7)$$

$$\text{Score} = 1/\text{Fitness function} \quad (8)$$

After selecting the best individuals of a population, a new generation of individuals have to be created from these to form a new subsequent population. This step of genetic operators can be separated into: elitism, crossover and mutation. The elitism stage is where the top individuals of the population are selected to continue as they are for the next generation. The crossover stage is similar to the breeding on the theory of evolution, where two parents are mated to create a child as a

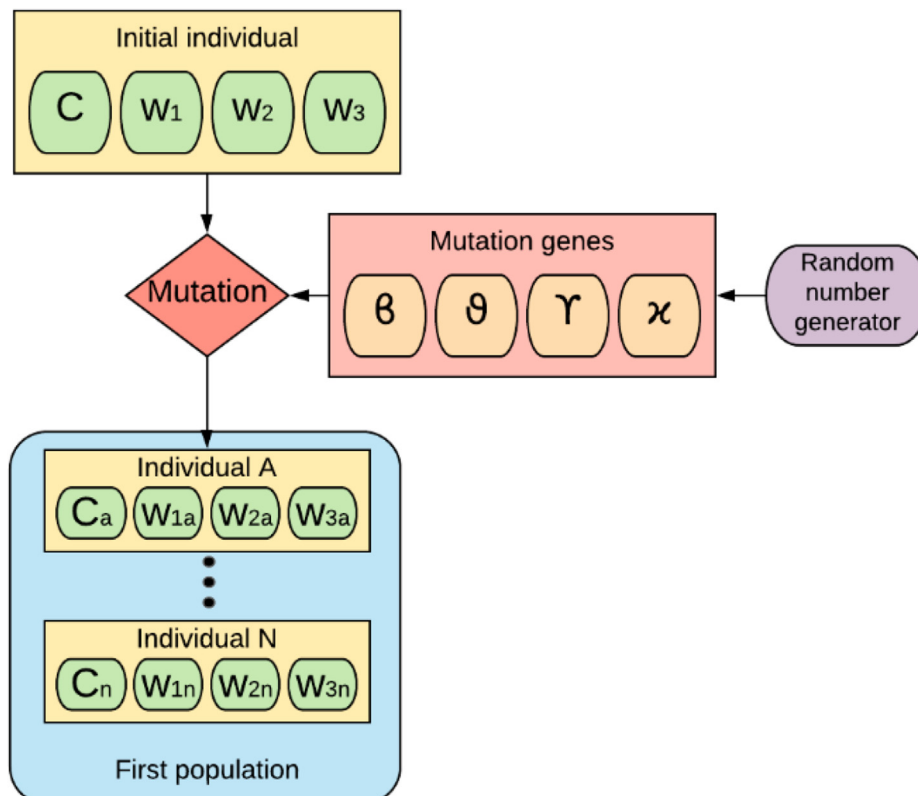


Fig. 2. Work flow of the initialization step on the genetic algorithm.

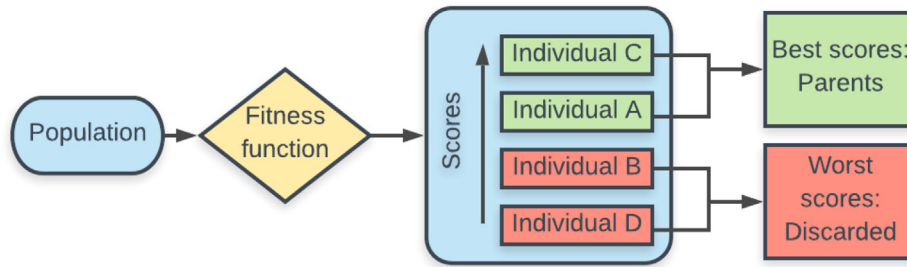


Fig. 3. Workflow of the selection step.

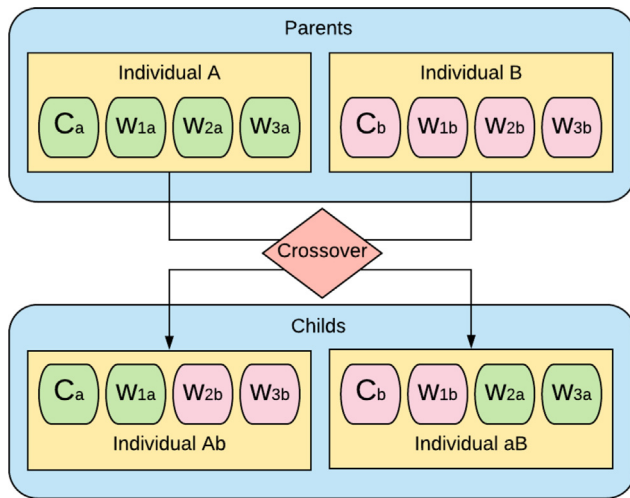


Fig. 4. Crossover stage, where a combination of two individuals genes create two new individuals.

combination of their genes. Fig. 4 shows the workflow of the crossover stage and how the child individuals are generated.

After the crossover, the remaining population is complemented by taking both the parents and children individuals and adding a mutation factor. Fig. 5 presents the workflow of the genetic operators stage, where a new population is generated to go through a new generation of the algorithm.

The algorithm ends using a termination criteria determined by: stagnation, objective found, or number of generations. The first one occurs when for a number of generations the best solution is the same, assuming that this is a maximum score. When setting the score function,

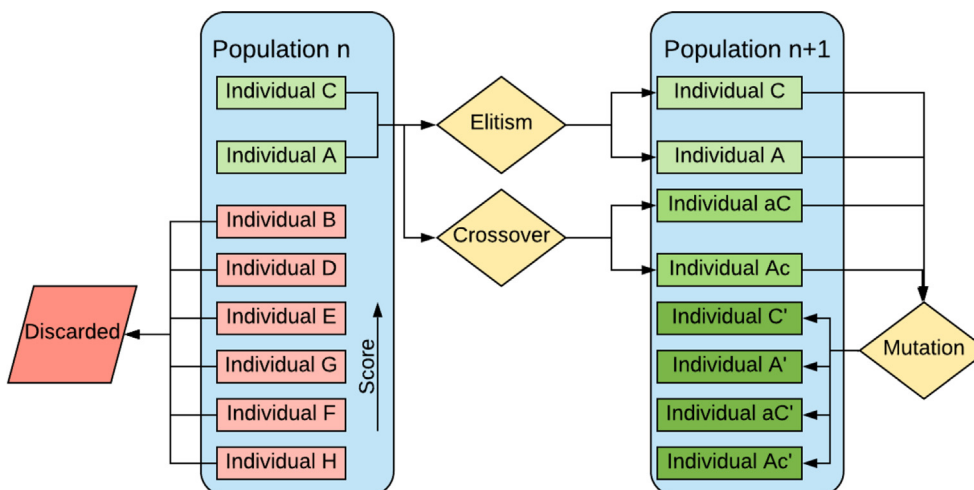


Fig. 5. Workflow of the genetic operators step where a new population is created.

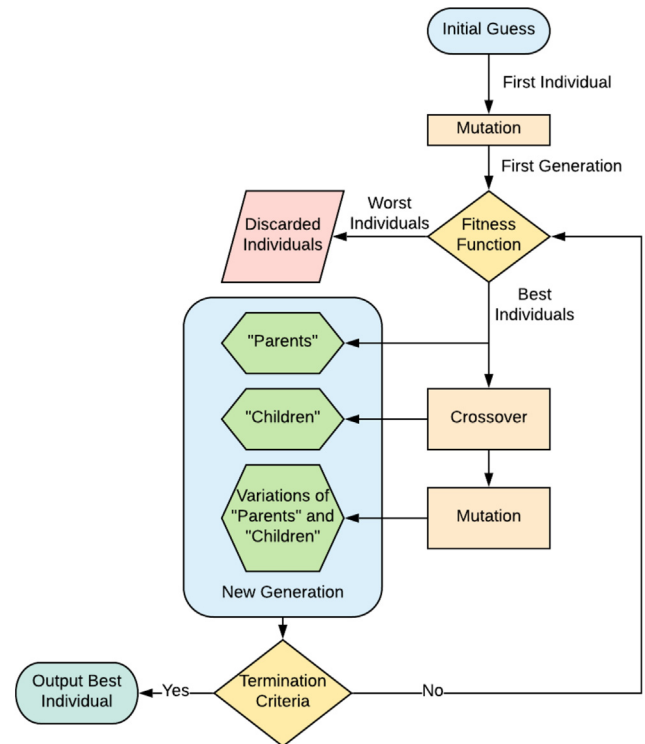


Fig. 6. Work flow of the developed genetic algorithm.

the human operator can determine a value that if met will end the algorithm, and that is the situation where the objective is found. It is also possible to set a maximum number of generations to end the GA. At the

Table 1
Citrus orchards characteristics (*FDT: Flying Dragon Trifoliar).

	Grove A	Grove B	Grove C
Tree variety	Hamlin/Valencia	Valencia	Valencia/Swingle
Tree rootstock	US897/US942 US802/ X639 FDT*/Swingle	Swingle	Swingle
Tree spacing	2.54 × 6.70 m	4.45 × 6.40 m	4.45 × 5.80 m
Number of trees	465	972	270

end, the function with the best score is selected as the optimal solution. Fig. 6 presents the workflow of the developed GA.

Since the UAV collected data is normally large (in this study over 500.000 values), to validate the solution the data was separated in 90% for GA training, and the other 10% for testing and validation. Using Eq. (4) as the objective function for the GA, where C is the camera coefficient and the fitness function is the absolute difference between the vNDVI and NDVI (Eq. (7)), the GA generated the weights as such to best optimize the function. To validate the proposed function, the value of the NDVI should be compared with the vNDVI in different conditions and plants (crops).

2.3. Experimental sites

To evaluate the proposed methodology and new index (vNDVI), the vNDVI must be tested and compared with the NDVI on different vegetation. Hence, three crops were selected as a case study: citrus, grapes and sugarcane. Three citrus orchards (groves) were selected to be used in this study, located at the Southwest Florida Research Center - University of Florida (SWFREC-UF), in Immokalee, FL, USA. For the citrus case, each tree was considered an individual in the GA. Table 1 presents information for each studied citrus field (grove).

The commercial vineyard (Lakeridge Winery & Vineyard) selected for this study, is located in Clermont, FL, USA. The field has an area of 4.73 ha (11.7 acres) containing Muscadine grape of Carlos variety. It contains 61 rows with vine spacing of 3.05 m × 6.1 m. The RGB and NDVI values were collected from each row (each vineyard row is an individual in the GA).

The sugarcane site is located in Clewiston, FL, USA and includes stage II and stage IV trials of sugarcane breeding programs (to evaluate new clones for disease resistance and higher yield). The sugarcanes were planted on November 2018, separated in 46 plots (stage II) and 12 clones in 6 replications (stage IV). The plot length was 10.7 m with 1.8 m separation between the tiers. Since some of the plots were too small on the orthomosaic, data were collected using several plots as one individual to gather both RGB and NDVI information.

2.4. UAV sensing systems

Two quadcopter UAVs (Matrice 210 and Phantom 4 Pro+, DJI, Shenzhen, China) and one hexacopter UAV (Matrice 600 Pro, DJI, Shenzhen, China) were used for image acquisition. For the UAV flight planning and mission control, the Pix4DCapture (Pix4D S.A., Prilly, Switzerland) software app was used on an iPad (Apple, Cupertino, CA, USA) connected to the remote controller of the UAVs.

Four sensing systems were used and evaluated: (i) an RGB (red, green and blue) camera (Zemuse X5S, DJI, WA, USA), attached to the Matrice 210; (ii) an RGB camera (Phantom 4 Pro + camera, DJI, WA USA), attached to the Phantom 4 Pro+; (iii) a multispectral camera (RedEdge-M, MicaSense, WA, USA) with five imaging sensors in blue (465–485 nm), green (550–570 nm), red (663–673 nm), red edge (712–722 nm), and near-infrared (820–1000 nm); and (iv) a Pika L 2.4 hyperspectral camera (Resonon, Bozeman, MT), attached to the Matrice 600 Pro. The hyperspectral camera covers a 400–1000 nm range divided in 150 bands. Table 2 presents the specifications of all the sensing systems utilized in this study. Each sensing system is equipped with a

GPS sensor to georeference each picture/data taken with its latitude and longitude.

The hyperspectral camera, Pika L 2.4 (Resonon, Bozeman, MT), uses a 17 mm Focal Length lens, field of view (FOV) of 17.6 degrees, and instantaneous field of view (IFOV) of 0.71 mrad. The camera has access to an inertial measurement unit IMU (DJI, Shenzhen, China) for the multi-rotor aircraft flight control, recording the sensor position and orientation.

3. Data collection

3.1. RGB data collection

RGB data were collected using both quadcopter UAVs (Matrice 210, and Phantom 4 Pro+); the Matrice 210 was equipped with the Zemuse X5S camera, and the Phantom 4 Pro+ with the Phantom 4 camera. A front overlap of 85% and a side overlap of 70% was set directly on the Pix4DMapper app. Data were collected at 122 m (400 ft) above the ground. The data were processed using the Pix4DMapper software (Pix4D S.A., Prilly, Switzerland) to stitch the collected UAV images into aerial maps. A 2,052 × 3,054 pixels (full resolution) map was generated for each of the following bands: red (R), green (G) and blue (B). The ground resolution was 1.5 cm. The RGB map was acquired from the Pix4DMapper processing mosaic.

3.2. Multispectral data collection

Multispectral data were collected using the DJI Matrice 210 quadcopter equipped with the Micasense RedEdge-M. The multispectral camera has its own software that works separately and can be configured using a wifi module accessing an IP address with the iPad. The camera is triggered also by the Micasense RedEdge-M software. For the multispectral data collection, an 80% for both front overlap and side overlap was used. Data were collected at 122 m (400 ft) above the ground. A calibrated reflection panel (CRP) designed specifically for this multispectral camera was used before and after the flight mission to provide radiometric calibration in order to compensate for sensor sensitivity, lighting, and atmospheric conditions.

The data were processed using the Pix4DMapper software (Pix4D S.A., Prilly, Switzerland) to stitch the collected UAV images into aerial maps. A 2,954 × 5,000 pixels (full-resolution) map was generated for each of the following bands: red (R), green (G), blue (B), red edge (RE) and near-infrared (NIR). The ground resolution for the multispectral camera was 5 cm. Additionally, an NDVI map was generated using a Python script.

3.3. Hyperspectral data collection

Hyperspectral data were collected using the DJI Matrice 600 equipped with the hyperspectral camera Pika L 2.4. The hyperspectral camera also has its own software and works separately from Pix4D. A front overlap of 85% and side overlap of 70% were used. Data were collected at an altitude of 60.96 m (200 ft) above the ground. A white calibration tarp was placed in the region of data collection to be used to calibrate the hyperspectral data collected.

The hyperspectral data were calibrated and analyzed using the Spectronon software (Spectronon Pro, Resonon, Bozeman, MT). The Georectification and Radiometric corrections were performed using the Spectronon Pro software, to get the GPS/IMU and radiometric data. The regions of interest (RoI) were manually selected based on each interest tree position and the hyperspectral wavelengths data were collected to be used as a reference data for the multispectral camera.

3.4. Citrus tree detection

To correct the GPS errors and correctly georeference the developed

Table 2
Specifications of the UAV-based sensing systems.

Sensing systems	Resolution	Pixel resolution at 122 m (400 ft) flight	Focal Length	Horizontal FOV	Vertical FOV	Diagonal FOV
RGB Zenmuse X5S	5,280 × 3,956 pixels (21 megapixels)	2.2 × 1.9 cm	15 mm	60.51°	35.83°	58.1°
RGB Phantom 4 Pro +	5,472 × 3,648 pixels (19.96 megapixels)	1.2 × 1.2 cm	24 mm	30.75°	20.77°	36.57°
Multispectral RedEdge-M	1,280 × 960 pixels (1.2 megapixels)	7.5 × 9.9 cm	5.4 mm	47.9°	36.9°	58.1°
Hyperspectral Pika L 2.4	Spectral Res: 2.1 nm		17 mm	FOV : 17.6 deg IFOV: 0.71 mrad		

orthomosaic maps generated from different sensing systems (e.g., RGB and multispectral cameras) with different resolutions and sizes, ground control points (GCPs), which are ground markers, were utilized. Using this technique, each tree position was corrected in all orthomosaic maps.

An algorithm was developed in Python, based on Ampatzidis and Partel (2019), to detect and geo-locate citrus trees and measure each tree’s canopy area. This algorithm utilizes a Faster-RCNN (Ren et al., 2015), instead of a YOLO (Redmon and Farhadi, 2018) used by Ampatzidis and Partel (2019). The Faster-RCNN was trained on 1,229 cropped images of other citrus orchards and blocks. The Faster R-CNN based algorithm has two main steps; a neural network (Region Proposal Network -RPN): (a) proposes for each candidate object in the image a bounding-box that contains said object(s) (e.g. a tree); and (b) extracts features using region of interest (ROI) from each candidate bounding-box and performs the final classification.

For each tree bounding box, the average of red, green and blue from the RGB images were retrieved. Using the georeference created by the ground control points inside the images, the average value of the NDVI was also calculated. Table 3 presents the number of trees and the number of detected trees, by the developed algorithm, for each grove. Fig. 7 shows an example of the resulting bounding-boxes for each tree on part of grove A.

On all citrus orchards (groves), the algorithm detected and counted 1,641 trees, and for each individual tree, using the bounding box from the detection, the average values of red, green and blue were collected and stored. With the references of each GCP from the images, the same bounding boxes are used on the NDVI map (generated by the multispectral camera) to collect their average NDVI values.

4. Experimental design

Three experiments were developed in this study to evaluate the proposed vNDVI. Fig. 8 summarizes all three experiments.

4.1. Experiment I

The experiment I evaluates the accuracy of the multispectral camera to produce an NDVI map. In this experiment, the NDVI map created by the multispectral camera was compared with the NDVI map generated by the hyperspectral camera, which has a higher resolution on the spectrum and can be used as a ground truth for the NDVI values. This “hyperspectral NDVI” map was compared with an NDVI map developed by the multispectral camera in a citrus field.

To ensure the same weather conditions, both flights were done one after the other with a few minutes in between them. On grove A, 100

Table 3
Citrus orchards (fields) detections by the Faster R-CNN.

	Grove A	Grove B	Grove C	Total
Number of trees	465	972	270	1707
Tree detection by the Faster-RCNN	463	921	257	1641
Precision of detection	99.57%	94.75%	95.18%	96.13%



Fig. 7. Example of Faster R-CNN tree detection on part of Grove A.

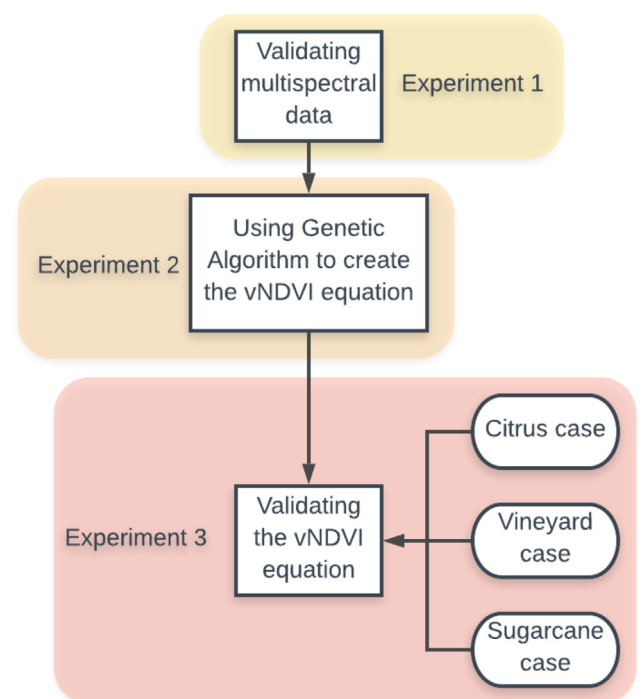


Fig. 8. Experimental design.

citrus trees were selected to retrieve their average NDVI value from both NDVI maps generated by the hyperspectral and multispectral cameras. In the “hyperspectral NDVI” map, each tree was manually selected using the Spectron software. In the “multispectral NDVI” map, a manual tool was developed to select an area of interest (individual trees) and retrieve the NDVI information (Python script). With

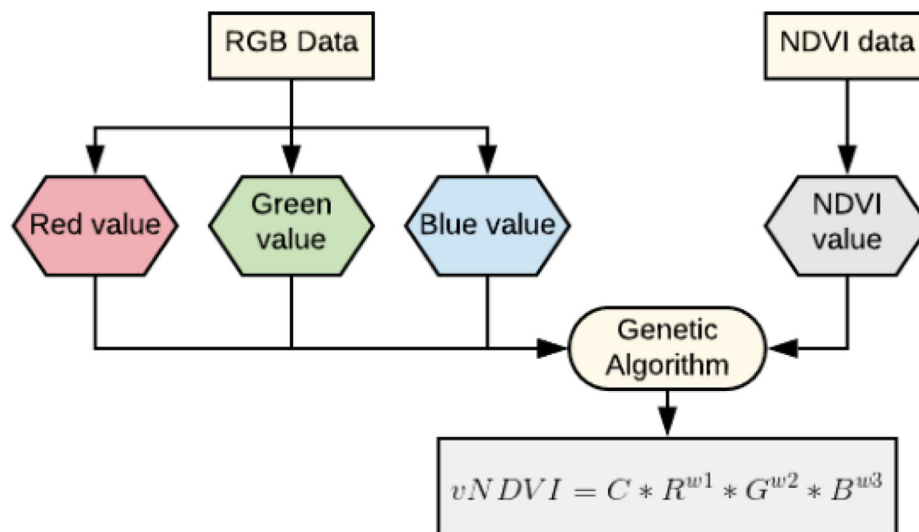


Fig. 9. Workflow of Experiment II.

this tool each tree average NDVI value was calculated.

To collect the NDVI data for all 1,641 trees (all groves), a methodology to detect trees in the RGB orthomosaic was used, and a georeference to the NDVI map was performed. Since only the multispectral camera (and not the hyperspectral) has sensors to georeference each image and can generate an orthomosaic for NDVI to be used, the multispectral camera was chosen over the hyperspectral to be used in the following experiments of this study.

4.2. Experiment II

In experiment II, the vNDVI equation was generated utilizing the multispectral data from all fields (three citrus groves, one vineyard and one sugarcane field). The RGB data from the multispectral camera were used as input to the proposed GA, with the NDVI values as the objective output, creating the vNDVI formula (Eq. (4)). Fig. 9 presents the process of experiment II.

4.3. Experiment III

In experiment III, the vNDVI was compared with the NDVI in three case studies (crops): citrus, vineyard and sugarcane. In this experiment, the vNDVI was calculated by the use of two uncalibrated RGB cameras (the Zenmuse X5S and the Phantom 4 Pro +), and the NDVI by the use of the multispectral camera RedEdge-M. The objective of this experiment was to define the camera coefficient for an uncalibrated RGB camera, as well as validate the vNDVI for multiple crops.

To collect data of each individual tree on the citrus case study, for each RGB orthomosaic, the developed Faster-RCNN detected the canopy for each tree and saved the information of both location and average pixel values of RGB for the bounding box. The location for each tree was then used to collect the same values for each bounding box on the multispectral map (for comparison purposes). With both values, the equation developed in experiment 2 was evaluated by comparing the NDVI with the proposed vNDVI. The difference in the values gave the camera coefficient for these uncalibrated cameras.

For the vineyard case study, each row of vines was selected manually and the average of the NDVI and vNDVI were compared for each individual row. A total of 50 rows were selected in this study.

For the sugarcane case study, each small field was selected as an individual, where 20 groups of plots were selected to be compared. Fig. 10 shows an example of the orthomosaic of the three crops.

4.4. Evaluation metrics

To evaluate the proposed vNDVI developed in this study, the following evaluation metrics were used: coefficient of determination (R^2), mean absolute error (MAE), and mean percentage error (MPE). The coefficient of determination is the squared Pearson correlation coefficient between the NDVI and the vNDVI as a measurement of the linear association between the two values; MAE is the mean of the absolute difference between NDVI and vNDVI; MPE is the mean error between the NDVI and vNDVI measurements (Eq. (9)).

$$Error = \text{Absolute}(NDVI - vNDVI)/NDVI \quad (9)$$

5. Results and discussion

5.1. Experiment I

After flying on grove A with both the hyperspectral and multispectral cameras (in similar weather conditions), the NDVI values of 100 trees were collected and compared (for both sensing systems). For visualization purposes, Fig. 11 shows an example of comparison between the data of 35 randomly selected trees. It can be seen that the multispectral camera underestimates the value of the NDVI compared to the hyperspectral camera.

On all 100 trees, the multispectral data presented a MAE of 0.05, with a MPE of 5.73%, which is usually by underestimating the value measured by the hyperspectral data. This low error shows that the use of the multispectral camera is appropriate for this study.

5.2. Experiment II

The multispectral data of all three study cases were used to create the formula for the vNDVI. For each map file, a sampling of every 4th pixel on the image was selected in order to reduce the size of the dataset, and the values of red, green, blue and NDVI were collected and stored. For all the maps used, over 1,000,000 pixel values were collected, containing vegetation, buildings, roads and lakes. These values were used in the GA to define the weights for the vNDVI (Eq. (4)), as presented in Eq. (10). For all of the values collected, 90% were used for training with cross-validation and 10% used for testing.

$$vNDVI = 0.5268 * (red)^{-0.1294} * (green)^{0.3389} * (blue)^{-0.3118} \quad (10)$$

Even though the same camera was used, the camera coefficient for Eq. (10) is different than 1 as the RGB sensors are not the same as the

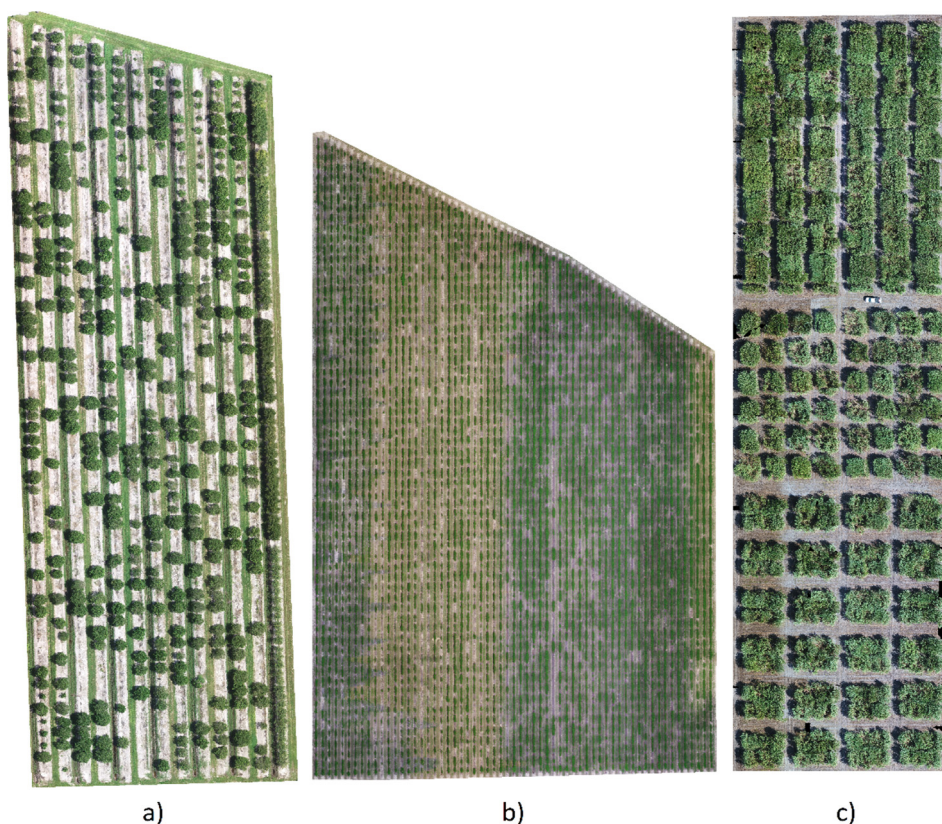


Fig. 10. Orthomosaic maps of: (a) citrus grove, (b) vineyard, (c) sugarcane plots.

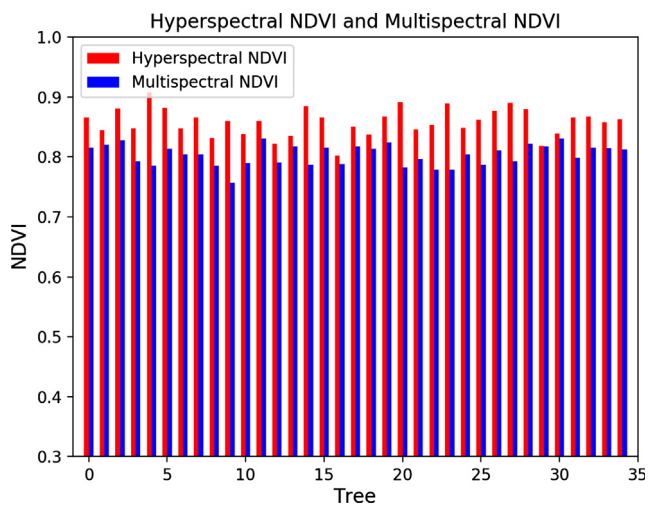


Fig. 11. Comparison between Hyperspectral NDVI and Multispectral NDVI in 35 randomly selected trees.

multispectral sensors in the camera. Fig. 12a presents the comparison between the pixel value for NDVI measured by the multispectral camera and the vNDVI created by the GA (example of 39 randomly selected pixels), while Fig. 12b presents the percentage error for each measurement.

The values for vNDVI from the testing dataset in this experiment presented a MAE of 0.042, with a MPE of 7.51%. The larger errors found on soil pixels, where the NDVI values were low (and not very accurate). Since the vNDVI formula is designed for vegetation, it get larger errors in soil. The R² value found using the Pearson correlation was 0.85 (Fig. 13), which indicates a good correlation between both measurement methods.

5.3. Experiment III

5.3.1. Citrus case

To get the RGB values of each tree in the bounding box (tree detections generated by the Faster R-CNN), a smaller box is used in the center of the bounding box to ensure that mostly pixels from the tree canopy (and not soil) were selected. The vNDVI was calculated from the RGB maps using the formula found in experiment II (Eq. (10)), and compared with the NDVI (measured by a multispectral camera) to define the camera coefficient using Eq. (5). The camera coefficient for the uncalibrated RGB cameras used was found to be:

$$C = NDVI / (red^{-0.1294} * green^{0.3389} * blue^{-0.3118}) = 0.5847 \quad (11)$$

Fig. 14a presents an example of the comparison between the NDVI (measured by a multispectral camera) and vNDVI (measured by an RGB camera) for 35 randomly selected citrus trees, while Fig. 14b shows the error in percentage between both measurements.

The vNDVI for an uncalibrated RGB camera resulted in a MAE of 0.021, with a MPE for the estimation of 2.75% (compared to the NDVI). The R² between both measurements was 0.79 (Fig. 15a). For the same detections, the correlation between VARI and NDVI was also retrieved to compare the accuracy of the VARI in predicting NDVI values. VARI was not developed to predict NDVI values, but both VARI and NDVI were created to evaluate crop health (as crop health indices), and hence, it is expected that both indices will have a good correlation. Fig. 15b shows the VARI and NDVI correlation, which found a R² of 0.65, much lower than the vNDVI (R² of 0.79) (Fig. 15a). Since NDVI is mostly used as a crop health index, a higher correlation shows that the vNDVI is better suited than VARI for that same purpose.

Fig. 16 presents a comparison of the NDVI, VARI, and vNDVI maps for the grove A (VARI and vNDVI maps created by using the Phantom 4 Pro + RGB camera).

From Fig. 16, it can be seen that the values for the trees in the NDVI and vNDVI are similar. Fig. 16 also shows that while both are created

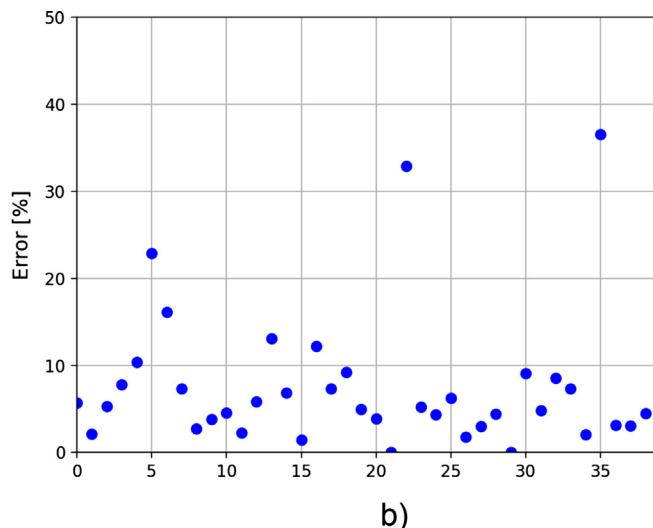
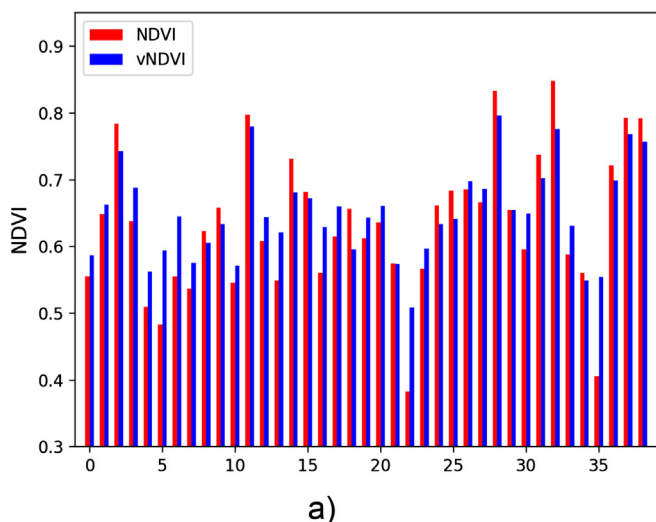


Fig. 12. (a) Comparison between 39 randomly selected pixels containing vegetation, soil and water for vNDVI (measured by an RGB camera) and NDVI (measured by a multispectral camera); (b) percentage error for each measurement.

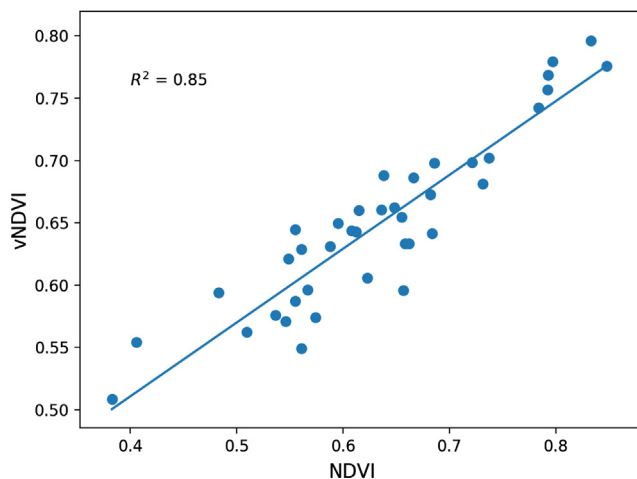


Fig. 13. Pearson correlation between vNDVI (measured by an RGB camera) and NDVI (measured by a multispectral camera) for each pixel value used from the three citrus groves maps.

from RGB images, the vNDVI map has a greater difference between vegetation and soil than the VARI map, which makes it easier to use as a vegetation fraction index as well.

5.3.2. Vineyard case study

Fifty rows of plants were used to compare the vNDVI (measured by an RGB camera) and NDVI (measured by a multispectral camera). The MPE was found as 11.57%, with a MAE of 0.092. Fig. 17a presents an example of the comparison between 30 randomly selected measurements (vine rows) and Fig. 17b the percentage error for each row.

It is important to note that in this case, the vNDVI underestimated the values in every row, which might be from the manual row selection procedure, which includes a human error (e.g., by not selecting the exact same area and/or by selecting more soil pixels which have lower values).

Fig. 18 presents the Pearson correlations between the vNDVI and NDVI, and between the VARI and NDVI. It can be seen that the vNDVI has a higher correlation (0.69) than the VARI (0.38).

5.3.3. Sugarcane case study

Twenty group of plots of sugarcane were selected to compare the

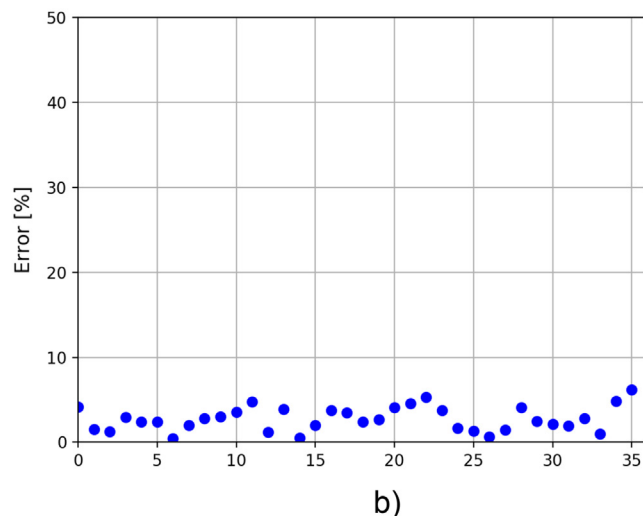
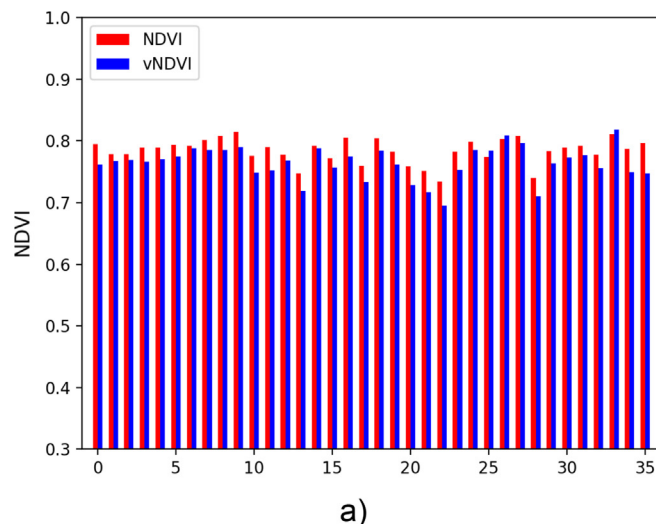


Fig. 14. Citrus case study: (a) Comparison between the NDVI (measured by a multispectral camera) and vNDVI (measured by an RGB camera) for an RGB uncalibrated camera (example of 35 randomly selected trees); and (b) the percentage error.

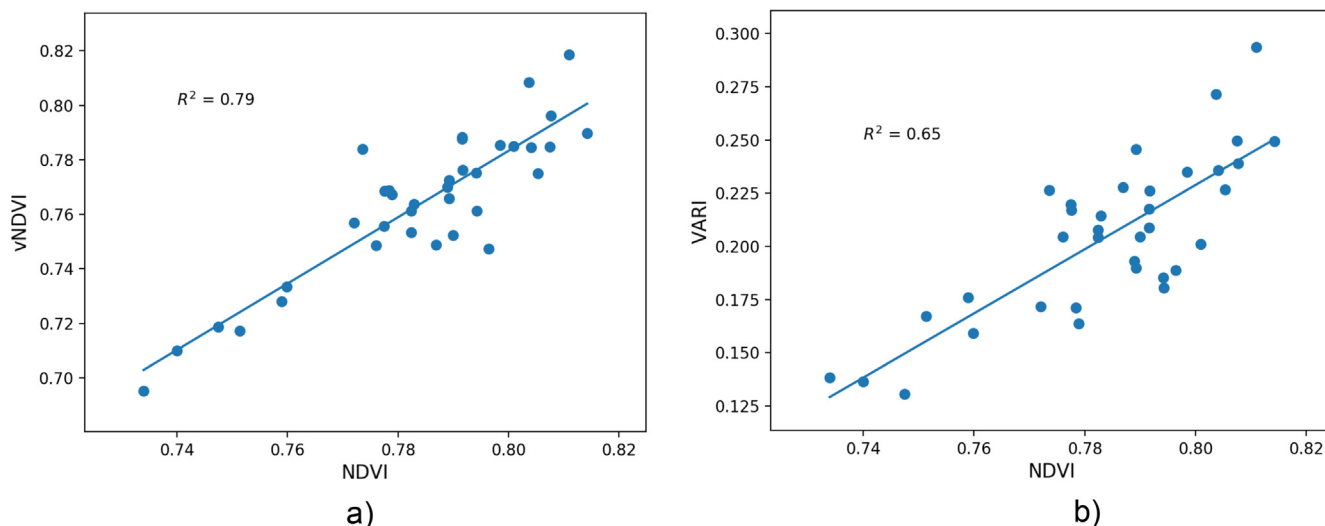


Fig. 15. Pearson correlation for the citrus case study between the: (a) NDVI and vNDVI, and (b) NDVI and VARI.

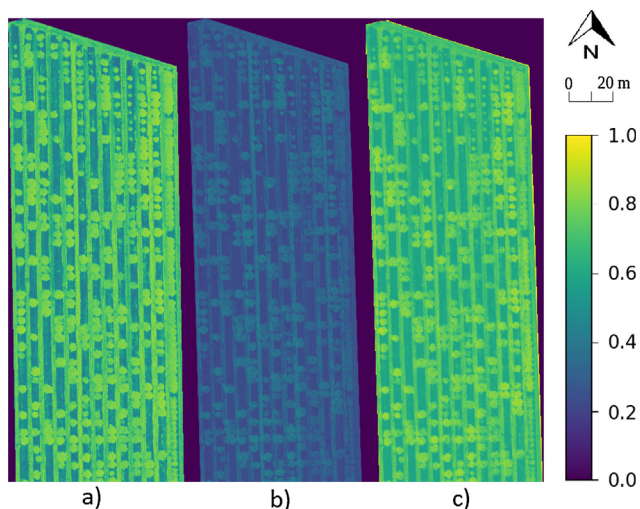


Fig. 16. Citrus case study: (a) NDVI, (b) VARI and (c) vNDVI for the citrus grove A.

vNDVI with the NDVI. The MPE found was of 8.07%, with a MAE of 0.052. Fig. 19a shows the comparison between the 20 measurements (groups of plots), and Fig. 19b presents the percentage error for each plot.

In this case study, the vNDVI overestimated the value of each sugarcane group of plots. It can also be seen that at the worst occasions, the percentage error was around 14%, which is still a good estimation for the NDVI. Fig. 20a presents the Pearson correlation between the NDVI and the vNDVI, which has a R^2 of 0.82, while Fig. 20b shows the correlation of NDVI and VARI with a R^2 of 0.77.

In all three crops, the vNDVI achieved a MPE of 6.89% and a MAE of 0.052, compared to the NDVI.

Much like the NDVI and other indexes, the vNDVI has some limitations as well, with the first being the effects of the weather and sunlight in the measurements. In different weather conditions the index could generate different measurements for the same plant. The second important limitation is that the vNDVI formula is not normalized, and as such could generate values higher than one on non-vegetation areas. On such occasion it is best to treat every value higher than one as one.

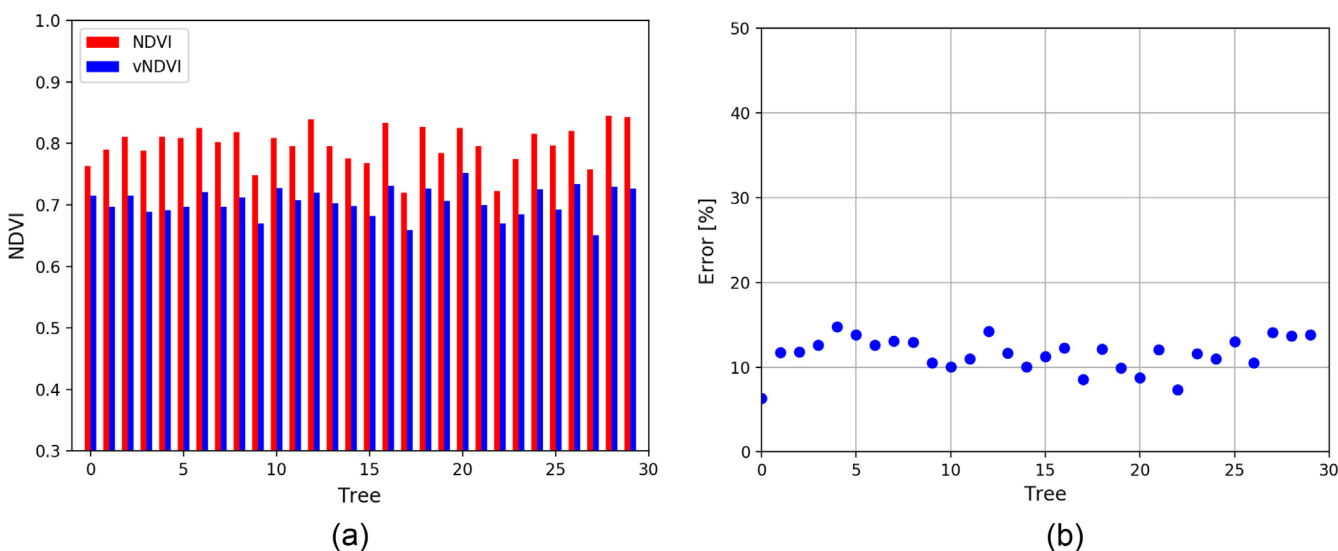


Fig. 17. Vineyard case study: (a) Comparison between vNDVI and NDVI for each vine row, (b) MPE of for each row.

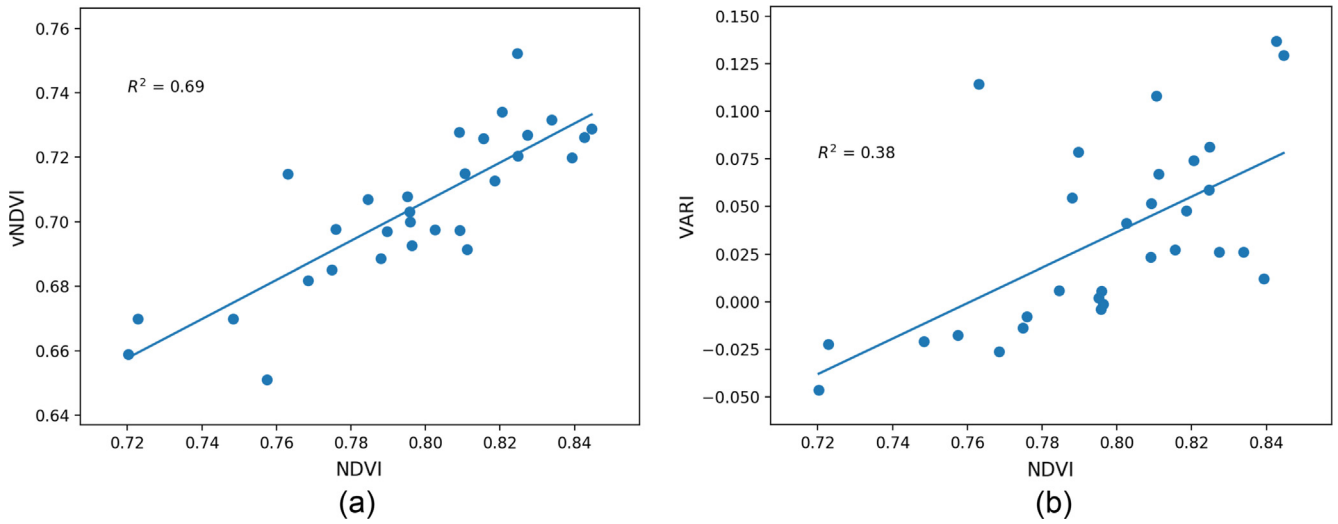


Fig. 18. Pearson correlation for the vineyard case study between the: (a) NDVI and vNDVI, and (b) NDVI and VARI.

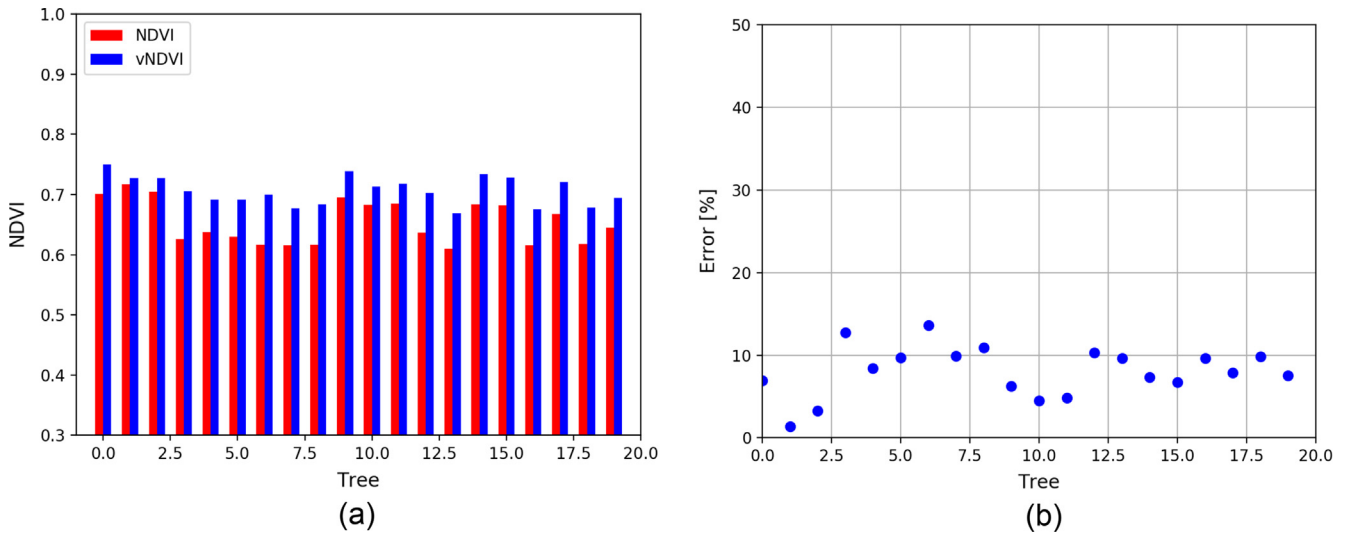


Fig. 19. Sugarcane case study: (a) Comparison between vNDVI and NDVI for each sugarcane plot, (b) MPE of the estimation for each plot.

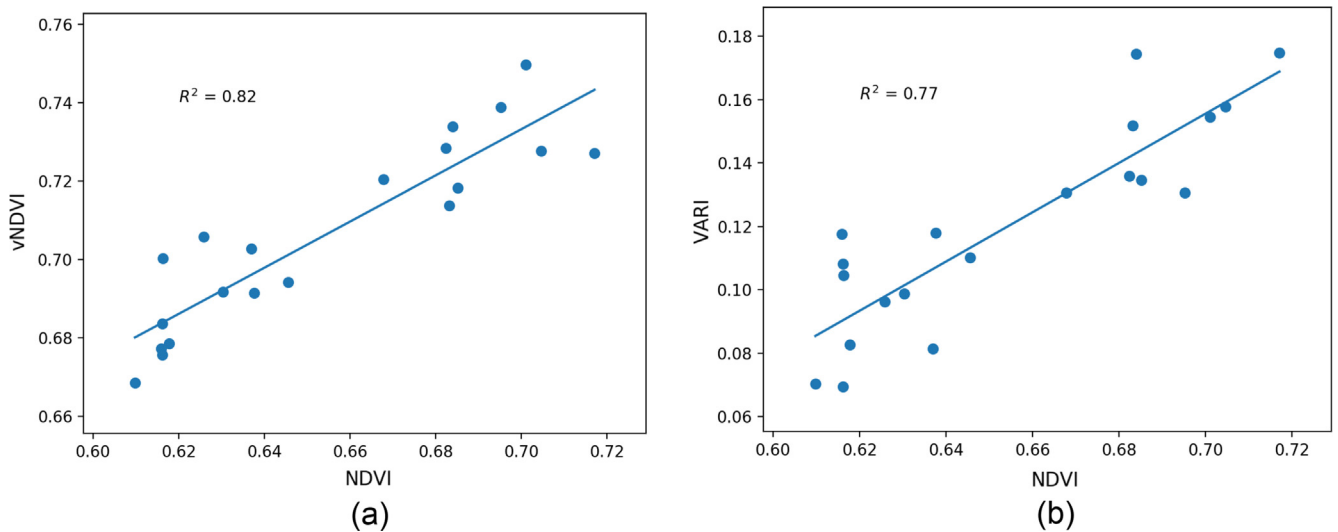


Fig. 20. Pearson correlation for the sugarcane case study between the: (a) NDVI and vNDVI, and (b) NDVI and VARI.

6. Conclusion

Vegetation indices and UAVs provide a rapid and low cost tool to assess vegetation information on arable and fruit trees crops. To generate most VIs, the use of relatively expensive and low spatial resolution multispectral or hyperspectral cameras is required. RGB cameras on the other hand provide a low-cost alternative (usually with a higher spatial resolution), but are limited on the data they can collect. In this study, a new visible NDVI (vNDVI) was developed, utilizing a genetic algorithm, to estimate NDVI values from RGB maps; a methodology to calibrate the vNDVI function for any RGB camera has been presented. The proposed vNDVI (measured from RGB cameras) accurately predicted NDVI values (measured by multispectral cameras) in three crops (citrus, grapes, and sugarcane) with an overall MPE of 6.89% and a MAE of 0.052. The vNDVI could be used as an alternative to multiple RGB-based VIs, with a better correlation to NDVI, and hence provide a more accurate crop health index. Scientists and developers could use and validate the proposed vNDVI in other crops or use the proposed GA-based methodology to develop similar VIs. The vNDVI can be specifically used with satellite data, where the multispectral images usually contain low spatial resolution data, compared to the high spatial and temporal resolution RGB data.

CRedit authorship contribution statement

Lucas Costa: Conceptualization, Methodology, Software, Validation, Formal analysis, Data curation, Writing - original draft, Visualization. **Leon Nunes:** Validation, Writing - review & editing, Visualization. **Yiannis Ampatzidis:** Conceptualization, Methodology, Validation, Formal analysis, Data curation, Writing - review & editing, Visualization, Supervision, Project administration, Funding acquisition.

Declaration of Competing Interest

The authors declare that they have no known competing financial interests or personal relationships that could have appeared to influence the work reported in this paper.

Acknowledgement

This material was made possible, in part, by a Cooperative Agreement from the U.S. Department of Agriculture's Animal and Plant Health Inspection Service (APHIS) and by the U.S. Department of Agriculture's Agricultural Marketing Service through grant AM190100XXXXG036. Its contents are solely the responsibility of the authors and do not necessarily represent the official views of the USDA.

Appendix A. Supplementary material

Supplementary data to this article can be found online at <https://doi.org/10.1016/j.compag.2020.105334>.

References

Abdulridha, J., Batuman, O., Ampatzidis, Y., 2019a. UAV-based remote sensing technique to detect citrus canker disease utilizing hyperspectral imaging and machine learning. *Remote Sens.* 11 (11), 1373.

Abdulridha, Jaafar, Ehsani, Reza, Abd-Elrahman, Amr, Ampatzidis, Yiannis, 2019b. A remote sensing technique for detecting laurel wilt disease in avocado in presence of other biotic and abiotic stresses. *Comput. Electron. Agric.* 156, 549–557. <https://doi.org/10.1016/j.compag.2018.12.018>.

Abdulridha, J., Ampatzidis, Y., Kakarla, S.C., Roberts, P., 2019c. Detection of target spot and bacterial spot diseases in tomato using UAV-based and benchtop-based hyperspectral imaging techniques. *Precis. Agric.* November, 1–24. <https://doi.org/10.1007/s11119-019-09703-4>.

Abdulridha, Jaafar, Ampatzidis, Yiannis, Ehsani, Reza, de Castro, Ana I., 2018. Evaluating the performance of spectral features and multivariate analysis tools to detect laurel wilt disease and nutritional deficiency in avocado. *Comput. Electron. Agric.* 155, 203–211. <https://doi.org/10.1016/j.compag.2018.10.016>.

Aleza, P., Juarez, J., Hernandez, M., Ollitrault, P., Navarro, L., 2012. Implementation of extensive citrus triploid breeding programs based on 4x × 2x sexual hybridisations. *Tree Genet. Genomes* 8, 1293–1306.

Ampatzidis, Y., Partel, V., 2019. UAV-based high throughput phenotyping in citrus utilizing multispectral imaging and artificial intelligence. *Remote Sensing* 11 (4), 410.

Ampatzidis, Y., Partel, V., Meyering, B., Albrecht, U., 2019. Citrus rootstock evaluation utilizing UAV-based remote sensing and artificial intelligence. *Comput. Electron. Agric.* 164 104900.

Ampatzidis, Y., Bellis, L.D., Luvisi, A., 2017. iPathology: Robotic applications and management of plants and plant diseases. *Sustainability* 9, 1010.

Arai, K., Gondoh, K., Shigetomi, O., Miura, Y., 2016. Method for NIR reflectance estimation with visible camera data based on regression for NDVI estimation and its application for insect damage detection of rice paddy fields. *Int. J. Adv. Res. Artif. Intell* 5 (11), 17–22.

Crommelinck, S., Bennett, R., Gerke, M., Yang, M., Vosselman, G., 2017. Contour detection for UAV-based cadastral mapping. *Remote Sens.* 9 (2), 171.

Cruz, A., Ampatzidis, Y., Pierro, R., Materazzi, A., Panattoni, A., De Bellis, L., Luvisi, A., 2019. Detection of grapevine yellows symptoms in *Vitis vinifera* L. with artificial intelligence. *Comput. Electron. Agric.* 157, 63–76.

Cruz, A.C., Luvisi, A., De Bellis, L., Ampatzidis, Y., 2017. X-FIDO: An effective application for detecting olive quick decline syndrome with deep learning and data fusion. *Front. Plant Sci.* 8, 1741.

Cuenca, J., Aleza, P., Vicent, A., Brunel, D., Ollitrault, P., Navarro, L., 2013. Genetically based location from triploid populations and gene ontology of a 3.3-Mb genome region linked to Alternaria brown spot resistance in citrus reveal clusters of resistance genes. *PLoS ONE* 8 (10) e76755.

Franzè, G.P.J., Woiski, E.R., Góes, L.C.S., 2017. HSV and NDVI Color Space Analysis and Sampling Procedure for Counting of Seedlings in Eucalyptus spp Plantations from High Definition Aerial Images. In: 2017 International Conference on Computational Science and Computational Intelligence (CSCI) (pp. 456–462). IEEE.

Gitelson, A.A., Merzlyak, M.N., 1996. Signature analysis of leaf reflectance spectra: algorithm development for remote sensing of chlorophyll. *J. Plant Physiol.* 148 (3–4), 494–500.

Gitelson, A.A., Kaufman, Y.J., Stark, R., Rundquist, D., 2002. Novel algorithms for remote estimation of vegetation fraction. *Remote Sens. Environ.* 80 (1), 76–87.

Harihara, J., Fuller, J., Ampatzidis, Y., Abdulridha, J., Lerwill, A., 2019. Finite difference analysis and bivariate correlation of hyperspectral data for detecting laurel wilt disease and nutritional deficiency in avocado. *Remote Sens.* 11(15), 1748; <https://doi.org/10.3390/rs11151748>.

Hunt Jr, E.R., Doraiswamy, P.C., McMurtrey, J.E., Daughtry, C.S., Perry, E.M., Akhmedov, B., 2013. A visible band index for remote sensing leaf chlorophyll content at the canopy scale. *Int. J. Appl. Earth Obs. Geoinf.* 21, 103–112.

Hunt, E.R., Hively, W.D., Fujikawa, S., Linden, D., Daughtry, C.S., McCarty, G., 2010. Acquisition of NIR-green-blue digital photographs from unmanned aircraft for crop monitoring. *Remote Sens.* 2 (1), 290–305.

Kaufman, Y.J., Tanre, D., 1992. Atmospherically resistant vegetation index (ARVI) for EOS-MODIS. *IEEE Trans. Geosci. Remote Sens.* 30 (2), 261–270.

Kussul, N., Lavreniuk, M., Skakun, S., Shelestov, A., 2017. Deep learning classification of land cover and crop types using remote sensing data. *IEEE Geosci. Remote Sens. Lett.* 14 (5), 778–782.

LeCun, Y., Bengio, Y., Hinton, G., 2015. Deep learning. *Nature* 521 (7553), 436.

Luvisi, A., Ampatzidis, Y.G., De Bellis, L., 2016. Plant pathology and Information Technology: Opportunity for management of disease outbreak and applications in regulation frameworks. *Sustainability* 8 (8), 831.

Mahlein, A.K., 2016. Plant disease detection by imaging sensors—parallels and specific demands for precision agriculture and plant phenotyping. *Plant Dis.* 100 (2), 241–251.

Malek, S., Bazi, Y., Alajlan, N., AlHichri, H., Melgani, F., 2014. Efficient framework for palm tree detection in UAV images. *IEEE J. Sel. Top. Appl. Earth Obs. Remote Sens.* 7 (12), 4692–4703.

Matese, A., Capraro, F., Primicerio, J., Gualato, G., Di Gennaro, S.F., Agati, G., 2013. Mapping of vine vigor by UAV and anthocyanin content by a non-destructive fluorescence technique. In: Precision agriculture 2013 (pp. 201–208). Wageningen Academic Publishers, Wageningen.

Mckinnon, T., Hoff, P., 2017. Comparing RGB-based vegetation indices with NDVI for drone based agricultural sensing. *Agribotix. Com* 1–8.

Pajares, G., 2015. Overview and current status of remote sensing applications based on unmanned aerial vehicles (UAVs). *Photogramm. Eng. Remote Sens.* 81 (4), 281–330.

Panda, S.S., Ames, D.P., Panigrahi, S., 2010. Application of vegetation indices for agricultural crop yield prediction using neural network techniques. *Remote Sens.* 2 (3), 673–696.

Partel, V., Kakarla, S.C., Ampatzidis, Y., 2019a. Development and evaluation of a low-cost and smart technology for precision weed management utilizing artificial intelligence. *Comput. Electron. Agric.* 157, 339–350.

Partel, Victor, Nunes, Leon, Stansly, Phil, Ampatzidis, Yiannis, 2019b. Automated vision-based system for monitoring Asian citrus psyllid in orchards utilizing artificial intelligence. *Comput. Electron. Agric.* 162, 328–336. <https://doi.org/10.1016/j.compag.2019.04.022>.

Rabatel, G., Gorretta, N., Labbé, S., 2011. Getting NDVI spectral bands from a single standard RGB digital camera: a methodological approach. In: Conference of the Spanish Association for Artificial Intelligence. Springer, Berlin, Heidelberg, pp. 333–342.

Rambla, J.L., Gonzalez-Mas, M.C., Pons, C., Bernet, G.P., Asins, M.J., Granell, A., 2014. Fruit volatile profiles of two citrus hybrids are dramatically different from those of their parents. *J. Agric. Food Chem.* 62 (46), 11312–11322.

Redmon, J., Farhadi, A., 2018. Yolov3: An incremental improvement. arXiv preprint

- arXiv:1804.02767.
- Ren, S., He, K., Girshick, R., Sun, J., 2015. Faster r-cnn: Towards real-time object detection with region proposal networks. In: *Advances in neural information processing systems*, pp. 91–99.
- Rouse Jr, J.W., Haas, R.H., Schell, J.A., Deering, D.W., 1973. Monitoring the vernal advancement and retrogradation (green wave effect) of natural vegetation.
- Şahin-Çevik, M., Moore, G.A., 2012. Quantitative trait loci analysis of morphological traits in Citrus. *Plant Biotechnology Reports* 6 (1), 47–57.
- Santoro, F., Tarantino, E., Figorito, B., Gualano, S., D'Onghia, A.M., 2013. A tree counting algorithm for precision agriculture tasks. *Int. J. Digital Earth* 6 (1), 94–102.
- Shakoor, N., Lee, S., Mockler, T.C., 2017. High throughput phenotyping to accelerate crop breeding and monitoring of diseases in the field. *Curr. Opin. Plant Biol.* 38, 184–192.
- Singh, A., Ganapathysubramanian, B., Singh, A.K., Sarkar, S., 2016. Machine learning for high-throughput stress phenotyping in plants. *Trends Plant Sci.* 21 (2), 110–124.
- Wulder, M.A., White, J.C., Niemann, K.O., Nelson, T., 2004. Comparison of airborne and satellite high spatial resolution data for the identification of individual trees with local maxima filtering. *Int. J. Remote Sens.* 25 (11), 2225–2232.
- Zhang, B., Zhang, L., Xie, D., Yin, X., Liu, C., Liu, G., 2016. Application of synthetic NDVI time series blended from Landsat and MODIS data for grassland biomass estimation. *Remote Sens.* 8 (1), 10. <https://doi.org/10.3390/rs8010010>.